Editors' Suggestion

Time- and angle-resolved photoemission spectroscopy for the saddle-point excitons in GaAs

Hiroshi Tanimura [1] and Katsumi Tanimura [2]

[1] *Institute for Materials Research, Tohoku University, 2-1-1 Katahira, Sendai 980-8577, Japan*

[2] *The Institute of Scientific and Industrial Research, Osaka University, 8-1 Mihogaoka, Ibaraki, Osaka 567-0047, Japan*

(Received 10 February 2020; revised 11 July 2020; accepted 14 July 2020; published 30 July 2020)

The electronic structure and dynamics of saddle-point excitons formed under E_1-resonance excitation around 3.0 eV in GaAs have been studied using time- and angle-resolved photoemission spectroscopy. The momentum- and energy-resolved spectra of the exciton photoionization reveal that the exciton wave function is composed mainly of the electron-hole pair states at the wave number of 0.32 ± 0.04 Å^{-1} along the Γ-L direction of the bulk Brillouin zone. Time-resolved characteristics of the photoemission is featured by a bimodal decay in the femtosecond (fs) time frame with two different time constants of 11 ± 0.5 fs and 120 ± 10 fs. The short lifetime reflects the autoionization processes of coherently generated excitonic polarization to unbound electron-hole pair states, and the long time constant represents incoherent exciton formation by combination between unbound electron-hole pairs during relaxation. The momentum- and energy-resolved features of photoemission from the exciton are governed by recoil effects of the conjugated holes that restore the valence-band states.

DOI: 10.1103/PhysRevB.102.045204

I. INTRODUCTION

Energies, intensities, and spectral line shapes in experimental optical spectra of semiconductors differ significantly from those predicted by the independent-quasiparticle picture (IQP) not only near the band-gap region at the M_0 critical point, but also in the higher energy regions around the M_1 and M_2 critical points of Van Hove singularities [1–4]. The excitonic effect of many-body interaction in electronic systems is the key concept to gain a deeper understanding of the optical properties of solids, thereby providing the foundation for a wide range of optoelectronic and photovoltaic applications.

Extensive studies have been carried out to elucidate the excitonic effect at the M_0 critical point near the Γ point, which forms distinctive excitonic absorptions below the band-gap energy E_G (the Γ excitons hereafter). Not only the spectroscopic characteristics but also the exciton dynamics have been studied in detail. Under laser excitation at the exciton resonance, the light field induces, beyond the linear regime of optical-solid interaction, an optical polarization that is directly proportional to the exciton wave function [5]. Ultrafast dynamics of dephasing and scattering processes of the coherent excitonic polarization in semiconductors have been studied extensively, and detailed knowledge of exciton dynamics in the coherent regime has been obtained [5–8].

The excitonic effects at the higher energy region above E_G have also been studied extensively. The imaginary parts of the dielectric functions $\epsilon(\omega)$ of diamond- and zinc-blende-type semiconductors increase above E_G to the peaks related to the E_1 transitions, showing a characteristic feature that it rises slowly as the photon energy increases to the E_1 peak and decreases sharply for the energy above the peak [1]. The E_1 (and $E_1 + \Delta_1$) transitions in the optical spectra have been attributed to the transitions related to the M_1 (saddle-type) critical points along the Λ direction of the Brillouin zone (BZ) based on band-structure calculations [1,3,4,9–13]. However, the experimental line shape of the E_1 transitions deviates significantly from that expected for M_1 critical points of Van Hove singularities. Based on extensive theoretical studies to elucidate the effect of the Coulomb interaction between electron and hole at the M_1 critical point, the discrepancies have been explained by excitonic effects at M_1 critical points [1,9]. Such excitons occurring at saddle points are known as the saddle-point excitons (SPEs) [1,3].

The spectral line-shape analysis of the E_1 transitions was carried out for many crystals of tetrahedrally bonded semiconductors in the group-IV, -III-V, and -II-VI families [9–13]. For GaAs, a prototypical direct-gap semiconductor, the spectral line shape of the E_1 transition has been analyzed by several authors [10–12]. Lautenschlager *et al.* have analyzed the second-derivative spectrum $d^2\epsilon(\omega)/d\omega^2$ for GaAs, and have shown that the spectrum of the E_1 (and also at the $E_1 + \Delta_1$) transition below room temperature is best fitted by a Lorentzian interacting with a continuum of interband transitions, which has been interpreted in terms of Fano interference [12,14,15]. They also showed that the line shape of two-dimensional critical point gives best representation for the E_1 transition above room temperature, suggesting a temperature-dependent crossover from excitonic to interband transitions at the E_1 critical point in GaAs.

Theoretically, rapid developments of efficient computational techniques have made it possible to investigate theoretically excitonic effects on the optical spectra of real materials from first principles [16–20]. Extensive calculations of exciton effects on the dielectric function have largely corrected the discrepancies between theoretical and experimental $\epsilon(\omega)$ spectra in many crystals, substantiating the important roles of excitonic effects in the high-energy region above E_G. Experimentally, however, the methods to study excitonic effects in the high-energy region have been limited to phenomenological line-shape analysis of $\epsilon(\omega)$. This limitation has prevented

us from gaining deeper understanding of the SPEs in semiconductors, and has kept the following fundamental questions unanswered. The first is what the wave functions of SPEs are. The assignment of the wave vectors at which the E_1 transition occurs has largely relied upon the band-structure calculations. The precise experimental determination of the wave vectors for interband critical points is important to elucidate the excitonic effect associated with Van Hove singularities. For this purpose, an introduction of a momentum-resolved spectroscopy method is crucial. The second is how long the lifetimes of SPEs are. For the Γ excitons, the dephasing time of laser-induced excitonic polarization in the picosecond range have been observed at low temperatures [6–8]. As the SPE is the bound state immersed in the continuum of uncorrelated electron-hole pair states, the dephasing process will be qualitatively different from those of the Γ excitons. The dynamical response of excitonic polarization associated with SPEs yields important knowledge to elucidate the electronic interaction of high-energy excitonic states with the continuum of unbound carrier states.

High-energy excitonic effects are more significant in two-dimensional materials, including graphene [21,22] and monolayer transition metal dichalcogenides [23], reflecting both intrinsic enhancement of Coulomb interactions and reduced screening. Therefore, elucidation of the high-energy excitonic effects becomes important for determining the unique features of the electronic properties of these two-dimensional materials. How to capture dynamical properties of SPE's experimentally, beyond spectral line-shape analysis, is now a crucial issue to be overcome.

In this paper, we study dynamics and electronic structures of the SPEs in GaAs, using time- and angle-resolved photoemission spectroscopy (TR-ARPES). One obvious reason is that TR-ARPES has a powerful capability of momentum-resolved spectroscopy. In addition to this, recent theoretical studies of exciton photoionization [24–28] have emphasized a unique capability of TR-ARPES to obtain a deeper insight into the wave functions of excitons, as briefly summarized below.

In ARPES for electronic-structure determinations of solids, one tacitly assumes a definite initial one-electron energy level $E_{\rm I}(\vec{k})$ from which electrons are photoionized ($\vec{k}$ being the wave vectors). In this case, the direct information of energy and wave vector of the $E_{\rm I}(\vec{k})$ can be obtained by measuring angle- and energy-resolved photoelectrons. The method can be used to study the normally unoccupied states (or the excited states) by applying pump and probe techniques with ultrashort light pulses. In Fig. 1(a), we show schematically the method to study the excited-state photoemissions for GaAs with the band structure obtained in Ref. [29]. Pump pulses (green arrow) induce interband transitions to inject electrons in the conduction band (CB) and generate holes in the valence band (VB). Probe light pulses then photoionize the hot electrons in the CB at a given time delay to generate photoelectrons specified by the momentum $\hbar\vec{k}$ and the kinetic energy $E_K(\vec{k})$. The wave vectors at which pump-induced interband transitions take place can be identified based on the momentum-resolved information of photoelectrons. The relation between $E_K(\vec{k})$ and $E_{\rm I}(\vec{k})$ referenced to the valence-band maximum (VBM) is given by

$$E_K(\vec{k}) = h\upsilon_{\rm probe} + E_{\rm I}(\vec{k}) - \Phi_{\rm vac}, \tag{1}$$

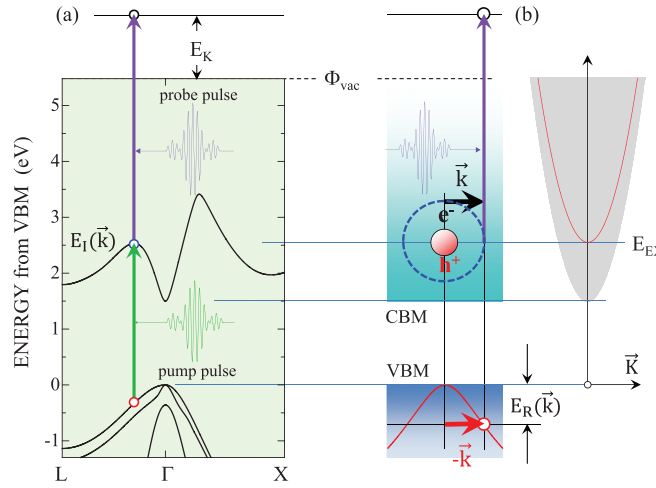

FIG. 1. (a) A schematic diagram of photoionization process of hot electrons populated on an unoccupied electronic state $E_{\rm I}(\vec{k})$ defined in the one-electron band picture. Solid black curves show the valence and conduction bands of GaAs calculated in Ref. [29], plotted with the experimental band-gap energy of 1.50 eV. The unoccupied conduction-band state is populated by a pump pulse (green arrow), and then photoionized by a probe pulse (violet arrow). (b) A schematic diagram of the photoionization process of excitons. The right panel shows the ground and excited states in a two-particle picture with the exciton state shown by the red curve. An electron is photoionized with a momentum $\hbar\vec{k}$ from an exciton by a probe pulse, while the conjugated hole restores the valence-band state with the recoil energy $E_R(-\vec{k})$. For other symbols used in the figure see the text.

where $h\upsilon_{\rm probe}$ is the probe-photon energy and $\Phi_{\rm vac}$ is the ionization energy. Then, the initial-state energy $E_{\rm I}(\vec{k})$ for photoemission can be determined.

However, such an initial one-electron energy level is indefinite, in principle, for photoionization of excitons, although the exciton itself has a well-defined energy level and a momentum as an eigenstate in photoexcited electron-hole systems [24–28]. An exciton is a bound state between an electron and a hole only in their relative space, being a superposition of various electron-hole pair excitations with amplitude $f(\vec{k}_e, \vec{k}_h)$, where $\vec{k}_e$ and $\vec{k}_h$ are wave vectors of the electron and hole in IQP band structure [2,30]. In the Wannier model, applicable for most inorganic semiconductors, an excitonic state $|ex\rangle$ with its center-of-mass wave vector $\vec{\rm K} = 0$ is defined as [2,30]

$$|ex\rangle = \sum_{\vec{k}} f(\vec{k}, -\vec{k})\hat{a}^+_{\vec{k}}\hat{b}^+_{-\vec{k}}|0\rangle, \tag{2}$$

where $\hat{a}^+_{\vec{k}}$ and $\hat{b}^+_{-\vec{k}}$ are creation operators of an electron with wave vector $\vec{k}$ and of a hole with wave vector $-\vec{k}$ in the IQP electronic structure, and $|0\rangle$ is the vacuum state.

In the photoionization processes of excitons, only electrons are emitted out of crystals, while the conjugate holes are left inside, and recoiled back to "original" valence-band states with the recoil energy $E_R(-\vec{k})$, as schematically shown in Fig. 1(b). Under momentum and energy conservations, the photoemitted electron from an excitonic state has the momen-

tum $\hbar\vec{k}$ and the energy $E_K(\vec{k})$ is given by

$$E_K(\vec{k}) = h\upsilon_{\text{probe}} + E_{\text{EX}} - E_R(-\vec{k}) - \Phi_{\text{vac}}, \quad (3)$$

where E_{EX} is the excitonic-state energy referenced to the VBM [25,26]. Therefore, the recoil of conjugates holes plays crucial roles in the photoionization of excitons; it governs the kinetic energy and momentum of photoemitted electrons. The energy $E_{\text{I}}(\vec{k})$ in Eq. (1) is now replaced with $E_{\text{EX}} - E_R(-\vec{k})$ in the case of exciton photoionization. As $E_R(-\vec{k})$ is determined primarily by the valence-band dispersion [25,26], the $E_K(\vec{k})$ in the exciton photoionization has no direct correlation with the conduction-band dispersion $E_{\text{I}}(\vec{k})$ of the IQP picture.

The theoretical consequence given by Eq. (3) gives us an experimental method to judge the importance of excitonic effects in optical transitions at interband critical points, different from the line-shape analysis extensively used previously. When any excitonic effects are weak enough at a given critical point, the initial state of hot-electron photoemission lies on the $E_{\text{I}}(\vec{k})$ predicted by the IQP band structure, while in the opposite case, the E_K can deviate significantly from that predicted by the $E_{\text{I}}(\vec{k})$.

More importantly, the photoemission intensity, specified by $\hbar\vec{k}$ and $E_K(\vec{k})$, in the exciton photoionization is proportional to $|f(\vec{k}_e, \vec{k}_h)|^2$. such that angle-resolved photoemission spectroscopy directly measures the amplitudes of momentum- and energy-resolved IQP Bloch functions of which the excitonic states are composed [24–28]. Therefore, TR-ARPES makes it possible, in principle, to determine experimentally the correlation between an excitonic state and the IQP Bloch states responsible for the excitonic state, which links directly the excitonic picture and IQP band structures. Furthermore, TR-ARPES is also useful to capture dark-exciton dynamics. Excitons are polaritons [31]. Therefore, only the excitonic states near $\vec{K} \approx 0$ can be captured in optical spectroscopy. On the other hand, photoemission spectroscopy can detect dark excitons with a finite $\vec{K}$ using the angle-resolved capability, as $h\upsilon_{\text{probe}}$ is totally off-resonant to the E_{EX} in usual cases. Such a demonstration has been reported for the excitons in Cu_2O in Ref. [32].

The method of TR-ARPES was applied, among others, to study dynamics of excitons in organic and inorganic solids [32–37], and several interesting aspects were revealed in exciton dynamics. We apply this method to study the SPEs associated with the E_1 critical point around 3.0 eV in GaAs [12]. Based on the capability of momentum-resolved spectroscopy mentioned above, we can obtain direct information of IQP Bloch states of which the SPEs are composed. Also, this method, with femtosecond (fs)-temporal resolution, allows us to study the dynamics of the SPEs, providing a breakthrough in methodology to study fundamental properties of high-energy excitons in much greater depth.

II. EXPERIMENT

GaAs single-crystals doped with Zn (3×10^{17} cm^{-3}) were cleaved under ultrahigh vacuum conditions ($<5 \times 10^{-11}$ Torr), and surface structures were characterized *in situ* using a scanning tunneling microscope. All samples used in this study showed well-ordered (1×1) surface structure with quasi-one-dimensional rows of top-most As atoms, and concentrations of surface point defects were typically less than 10^{-3} monolayers. A 76-MHz Ti-sapphire laser generated 50-fs laser pulses centered at photon energies from 1.4 to 1.60 eV. A portion of the fundamental output was frequency doubled to generate second-harmonic (2ω) pump pulses, while another portion of the fundamental output was converted to third-harmonic (3ω) pulses for probing photoemission. The cross-correlation trace between pump and probe pulses in a BBO crystal was well described by a Gaussian with a full width at half maximum of 75 ± 5 fs. Another laser system, consisting of a Ti-sapphire laser oscillator, a regenerative amplifier, and a tunable optical parametric amplifier was also used to generate 45-fs pump-laser pulses at photon energies between 1.7 and 2.5 eV. A portion of amplified fundamental (790 nm) was converted to 50-fs third-harmonic pulses for probing photoemission. The probe pulses passed a computer-controlled delay stage with a high precision to set the time delay (Δt) with respect to the pump pulses, and pump and probe pulses were aligned coaxially and focused on the sample surfaces at 45° to surface normal. Using a hemispherical electron analyzer operated in an angle-resolved lens mode, equipped with a two-dimensional image-type detector, photoelectron images were recorded as a function of the electron kinetic energy E_K and emission angle θ along the [001] crystal direction: surface normal photoemission was along the [110] crystal direction. The energy resolution using fs-probe light was 60 meV, while the angle resolution was $\pm 0.5^\circ$.

All measurements were made at 90 K. The pump-pulse fluence was set to give a typical excitation density ρ_0 less than 3×10^{17} cm^{-3}, which was evaluated using the formula $\rho_0 = F_p(1-R)\alpha$, with the photon fluence of pump pulse F_p, the reflectivity R and the absorption coefficient α at excitation photon energy ($h\upsilon_{\text{pump}}$). The ρ_0 gives the maximum value of the density of excited species with long enough lifetimes. For an excited state with a short lifetime τ, the density generated by a light pulse with a temporal width ω is reduced roughly by a factor τ/ω. For $\rho_0 = 3 \times 10^{17}$ cm^{-3}, the magnitude of the excitation density for the state with 10-fs lifetime is estimated to be about 5×10^{16} cm^{-3}, lower than Mott density in GaAs reported in Ref. [38]. For a pump-pulse fluence (typically 0.7 μJ/cm^2) to achieve the excitation density, any effects of lattice heating by excitation can be neglected (Probe-pulse fluences were less than 1/100 of those of pump pulses). Experimentally, we could confirm essentially no effects of laser-induced lattice heating by measuring the photoemission spectra from the electrons accumulated near the CBM at $\Delta t > 10$ ps when electrons injected by pump-laser pulses were thermalized [39]. At the time delays when the electrons are thermalized, the highest transient lattice temperatures may result by the energy transfer from electronic to lattice systems. The spectrum was well described by a Boltzmann distribution with the electron temperature of 90 K. The analysis of the CBM photoemission provides the definitive correlation between the measured kinetic energies of photoelectrons and the conduction-band states of GaAs [39].

In the present time-resolved photoemission measurements, the final-state energies reached by pump and probe pulses were limited to below 8 eV with respect to the Fermi level. The inelastic mean free path at the energy region is

typically 30 Å [40], which is substantially larger than the depth of the (1 × 1) surface layer of ∼1 Å [41]. Therefore, the bulk sensitivity is enhanced strongly, compared with normal ultraviolet photoemission spectroscopy probed by light with photon energy of typically a few tens of eV. The $E_K(\vec{k})$ of a photoelectron was referenced to the low-energy cutoff in a photoemission spectrum which corresponds to the vacuum level of a sample [42]. The relation between $E_K(\vec{k})$ and $E_I(\vec{k})$ of an IQP state referenced with the VBM is given by Eq. (1). For GaAs (110)−(1 × 1) surfaces, $\Phi_{vac} = 5.47$ eV [41,43]. As the $E_K(\vec{k})$ is dependent on $h\upsilon_{probe}$, it is useful to use $E_I(\vec{k})$ to characterize an initial state of photoemission in the spectra measured with different $h\upsilon_{probe}$. Furthermore, when we compare experimental results with theoretical band-structure calculations, the excess energy $E_{cb}(\vec{k})$ referenced to the conduction-band minimum (CBM) becomes more convenient [$E_I(\vec{k}) = E_{cb}(\vec{k}) + E_G$], as several band-structure calculations do not give the correct value of the band-gap energy. We use $E_K(\vec{k})$, $E_I(\vec{k})$, and $E_{cb}(\vec{k})$ to scale the photoelectron energy in the most suitable forms in respective figures.

III. EXPERIMENTAL RESULTS

Figures 2(a)–2(c) show the energy- and momentum-resolved (k-resolved) maps of photoemissions measured at Δt indicated in the figures, under excitation with $h\upsilon_{pump}$ at 2.30, 2.48, and 2.98 eV, respectively. In the figures, photoemission intensities specified by color scales are plotted as a function of electron momentum ($k_{||}$) parallel to the surface and energy of photoelectrons. The energy is scaled in terms of $E_{cb}(\vec{k})$, based on the precise determination of the CBM photoemission measured at $\Delta t = 10$ ps.

Figure 2(d) shows the relation between the bulk Brillouin zone (BBZ) and the surface Brillouin zone (SBZ) under the geometry for the measurements [39,44]; the [110] crystal axis is aligned along the surface normal, and the [110] and [001] axes define the detection plane. As the emission angle θ corresponds to $k_{||}$ along the $\bar{\Gamma}$-$\bar{Y}$($= \bar{X}'$) direction of the SBZ, the measured photoemission image represents a one-dimensional cut, along the $\bar{\Gamma}$-$\bar{Y}$ of the SBZ, of the two-dimensional projection of three-dimensional electron distributions. The projection has the following characteristics. First, all states along the Γ-K direction in the BBZ are projected at the $\bar{\Gamma}$, contributing to surface-normal photoemission. Second, the states along the Γ-L line in the BBZ are projected on the $\bar{\Gamma}$-$\bar{Y}$ direction with $k_{||}$ given by $k_{||} = k_L \cos(54.7^\circ)$, with k_L being the wave vector along the Γ-L direction. Third, the states along the Γ-X line in the BBZ are projected on the $\bar{\Gamma}$-$\bar{Y}$ direction with $k_{||} = k_X$, with k_X being the wave vector along the Γ-X direction. However, electron momenta perpendicular to the surface are zero for states along the Γ-X direction; they cannot be detected under the geometry.

The solid (broken) curve in Figs. 2(a)–2(c) is the CB dispersion along Γ-L direction (Γ-X direction) as a function of $k_{||}$, evaluated using the theoretical results obtained by the local-density approximation and pseudopotential method in Ref. [29]. The saddle point of the CB along the Γ-L direction is located at $k_{||} = 0.169$ Å^{-1}, which corresponds to $k_L = 0.292$ Å^{-1}, in this calculation. Therefore, photoemissions

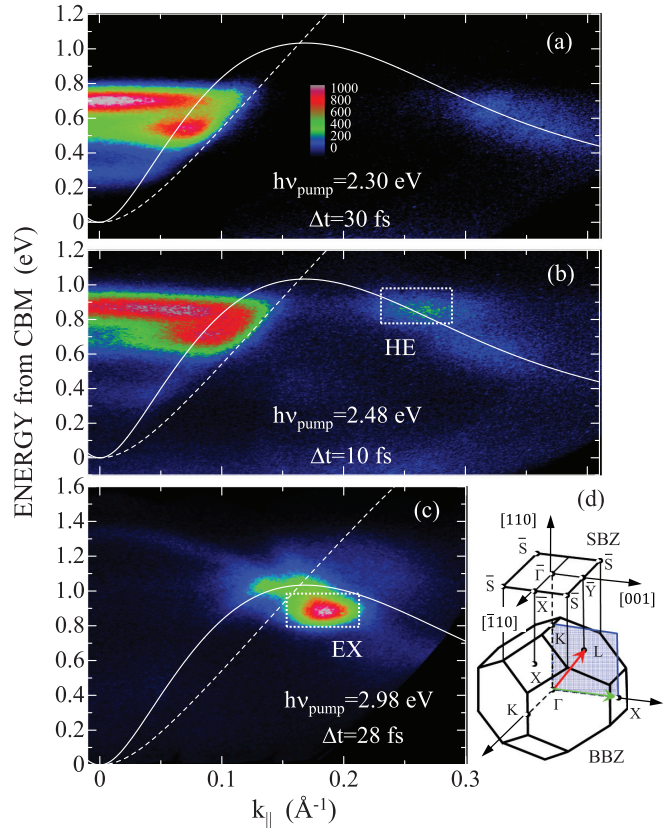

FIG. 2. (a)-(c) Photoemission images under excitation at 2.30 eV (a), 2.48 eV (b), and 2.98 eV (c). Photoemission intensities are plotted as a function of electron momentum ($k_{||}$) parallel to the surface and energy of photoelectrons. The energies of photoelectrons are scaled in terms of the energy E_{cb} of bulk conduction-band states referenced to the CBM, based on the precise determination of the CBM photoemission peak. The color scale specifying the photoemission intensity in (a) is common for (b) and (c). Samples were excited by s-polarized laser pulses, and images were measured at the time delay indicated in the figures. The solid and broken curves show the conduction-band dispersion along Γ-L and Γ-X directions, plotted as a function of $k_{||}$, based on the band-structure calculation in Ref. [29]. Panel (d) shows the relation between the bulk Brillouin zone (BBZ) and the surface Brillouin zone (SBZ) under the geometry of the present measurements: the [110] crystal axis is aligned along the surface normal, and the [110] and [001] axes define the detection plane.

with $k_{||} < 0.169$ Å^{-1} come from hot electrons injected in the Γ valley of the CB, while those with $k_{||} > 0.169$ Å^{-1} originate from the states outside the Γ valley. In the present configuration of photoemission measurements shown in Fig. 2(d), the states at the high-energy side of the L valley contribute to the photoemissions at the range $k_{||} > 0.169$ Å^{-1}; the L_1 point of the CB corresponds to $k_{||} = 0.556$ Å^{-1}, being outside of our detection window.

In Figs. 2(a) and 2(b), the initial populations of hot electrons are confined mostly in the Γ valley. This is reasonable, as the optical transitions from the VB to CB states are not possible energetically around the Λ for $h\upsilon_{pump} < 2.5$ eV. The energy distributions of hot electrons injected into the Γ valley show three peaks; they are 0.70, 0.55, and 0.26 eV

in Fig. 2(a). The three peaks correspond to the transitions from the heavy-hole, light-hole, and split-off valence bands to the CB states, and the momentum distributions of the peaks are governed by the selection rules of the optical transitions [39,45]. In Figs. 2(a) and 2(b), finite populations can be detected at $k_{||} > 0.169$ Å^{-1}, outside of the Γ valley. As identified previously [29,39,46], the hot-electron populations at the L valley for $h\upsilon_{\text{pump}} < 2.5$ eV are due to ultrafast momentum scattering of hot electrons photoinjected into the Γ valley. In both cases of Figs. 2(a) and 2(b), hot-electron distributions in the map of $k_{||}$ and E_{cb} are well registered on the dispersion curve of the CB in the IQP band structure.

However, when the same sample is excited with 2.98-eV photons, which is resonant with the E_1 transition in GaAs [12], the pattern of photoemission changes dramatically as shown in Fig. 2(c); one intense peak around $k_{||} = 0.183$ Å^{-1} and $E_{\text{cb}} = 0.88$ eV, denoted as EX, dominates over other features of photoemission. There are photoemission signals with weaker intensities near the saddle point at 1.03 eV along the Γ-L line of CB dispersion curve, which can be assigned to photoemissions from hot electrons in the CB. Importantly, the peak energy and momentum of EX photoemission deviate significantly from the CB dispersions predicted from the IQP band structure, revealing a unique feature of the EX photoemission.

In Fig. 3, temporal evolution of photoemission images under 2.48- and 2.98-eV excitation are compared. Figures 3(a)–3(f) show the results under 2.48-eV excitation. For hot electrons populated at the L valley by the intervalley scattering from the Γ valley, it is clear that the electron energy shows a low-energy shift, while the $k_{||}$ that gives the peak intensity becomes larger with increasing Δt. Therefore, they are relaxing towards the L_1 point along the CB-dispersion curve. As the intensity of hot-electron photoemission at the L valley increases with increasing Δt, hot electrons are accumulated in the L valley in the time frame of 200 fs. Exactly the same feature of hot electron relaxation under 2.30-eV excitation has been reported in Ref. [46]. On the other hand, as seen in Figs. 3(g)–3(l), which show temporal evolution of photoemission map under 2.98-eV excitation, the intensity of the EX peak is reduced significantly in the first 100 fs, as indicated by the color scale in each panel, with keeping the $k_{||}$ that gives the peak intensity almost unchanged. Careful inspections reveal that the magnitude of $k_{||}$ becomes *smaller* at larger Δt, and the peak energy of the EX photoemission displays collectively a *high-energy shift*; it is 0.88 eV at $\Delta t = 28$ fs, while it becomes 0.94 eV at $\Delta t = 94$ fs. These unique features of the EX photoemission are essentially different from those of hot electrons in the CB displayed in Figs. 3(a)–3(f).

We mention here another interesting feature in photoemission images under 2.98-eV excitation. As seen in Fig. 2(c) and 3(g)–3(i), a highly dispersive signal ($E_{\text{cb}} = 1.33$ eV at $k_{||} = 0$ Å^{-1}) can be detected in the $k_{||}$ ranging from 0 to 0.15 Å^{-1}. The signal is weak and short-lived; it disappears within 100 fs of excitation. The dispersive photoemission peaks could not be detected for excitation with $h\upsilon_{\text{pump}} < 2.5$ eV. We discuss the origin of the dispersive peak in the Appendix.

We carried out similar time- and angle-resolved photoemission measurement under 2.98-eV excitation using a different sample orientation where the detection plane is defined by the

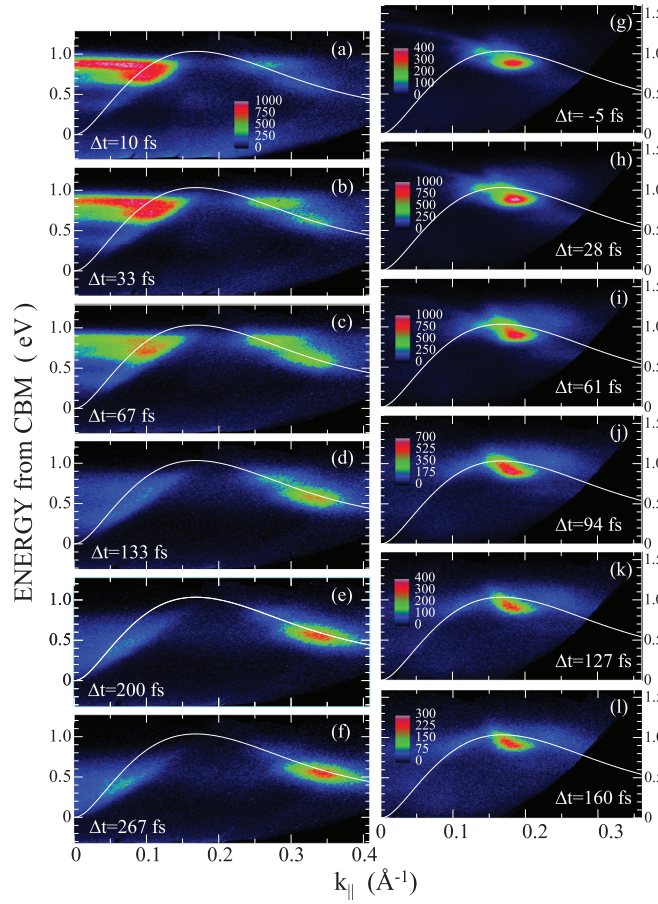

FIG. 3. Temporal evolution of photoemission images plotted as a function of $k_{||}$ and E_{cb} under 2.48 eV (a)–(f), and under 2.98 eV (g)–(l). Images were measured at Δt indicated in each panel. For (a)–(f), the color scale showing photoemission intensities is common, while different color scales were used for (g)–(l) in order to emphasize the EX-peak feature. The solid curve shows the conduction-band dispersion along the Γ-L line based on the band-structure calculation in Ref. [29].

[110] and [$\bar{1}$10] axes [see Fig. 2(d)]. In this case, off-normal emissions are characterized by $k_{||}$ along the $\bar{\Gamma}$-$\bar{X}$ direction of the SBZ, to which states along the Γ-X direction in the BBZ contribute with $k_{||} = k_X \sin(45°)$. However, we could not detect any intense peaks, similar to the EX photoemission, for the $k_{||}$ ranging from 0 to 0.30 Å^{-1}. Therefore, the state responsible for the EX photoemission (the EX state hereafter) is highly localized in the momentum space probed in the detection plane spanned by the [110] and [001] axes, which includes the states along the Γ-L direction of the BBZ.

In Fig. 4, the total intensity of EX photoemission is plotted by a solid black curve as a function of Δt. The total intensity was obtained by integrating photoemission signals with respect to $k_{||}$ and energy in the rectangle labeled EX in Fig. 2(c), which is specified by energy of 0.88 ± 0.09 eV and by $k_{||}$ of 0.183 ± 0.03 Å^{-1}. The maximum is reached at $\Delta t = 28$ fs, and the intensity is reduced significantly within 100 fs of excitation, leaving a slowly decaying component surviving until 500 fs. The changes in the peak kinetic energy of EX emission are also plotted as a function of Δt in Fig. 4.

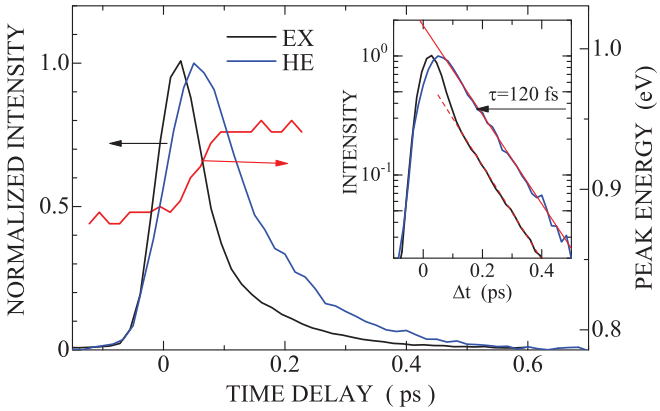

FIG. 4. The total intensity of EX photoemission under 2.98-eV excitation, integrated with respect to $k_{||}$ and energy in the rectangle labeled EX in Fig. 2(c), is plotted as a function of Δt by solid black curve, and is compared with temporal change in the intensity of hot electrons under 2.48 eV (blue curve), integrated with respect to $k_{||}$ and energy in the rectangle labeled HE in Fig. 2(b). The energy of EX photoemission peak is also plotted as a function of Δt by the solid red curve. The inset of the figure displays the intensities plotted in a semilogarithmic scale. The solid and broken red lines show single-exponential decays with the time constant of 120 fs.

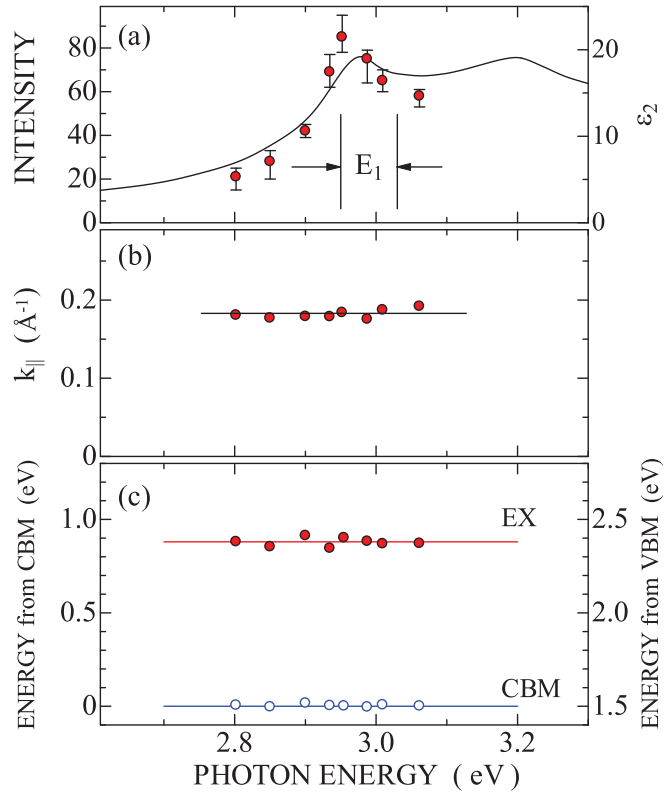

FIG. 5. (a) The EX-photoemission intensity as a function of pump-photon energy. For each pump-photon energy, the photoemission spectra were measured as a function of Δt, and the $(\Delta t)_M$ when the EX-photoemission intensity showed the maximum value was determined. Based on the data at $(\Delta t)_M$, the total intensity was evaluated by integrating the photoemission intensities with respect to $k_{||}$ and energy in rectangles as in Fig. 2(c). Thus determined total intensity was then normalized with respect to the photon fluence (number of photons per unit area) of pump and of probe pulses. Error bar stands for the estimated maximum error in determining total intensities of the results measured at least three different runs. The solid curve shows imaginary part of the dielectric function of GaAs at 253 K (after Ref. [12]). The energy range specified by the label E_1 corresponds to the range of E_1-transition energies at ~90 K taken from experimental results compiled in Ref. [12]. (b) The magnitude of $k_{||}$ that gives the peak of EX photoemission as a function of pump-photon energy. (c) The initial-state energies of the EX photoemission, red circles, and of the conduction-band photoemissions, blue circles, referenced to the CBM. The right-axis scale shows the initial-state energy referenced to the VBM.

The initial peak energy of 0.88 eV increases to 0.94 eV within 100 fs of excitation when the intensity is reduced sharply. The results shown in Fig. 4 indicate clearly that the EX mission consists of two different components; the fast-decay component has the peak energy of 0.88 eV, while the slow-decay component has the peak energy of 0.94 eV.

In order to compare the temporal change of the EX-photoemission intensity with that of the hot-electrons relaxing in the L valley, we integrated the hot-electron signals in the rectangle labeled HE in Fig. 2(b), which has the same energy range as that for EX photoemission, but a different $k_{||}$ range of 0.26 ± 0.03 Å^{-1}. The result is plotted by a solid blue curve in Fig. 4. In the inset of the figure, we compare the temporal changes of EX and hot-electron photoemission intensities in a semilogarithmic scale. The decay of hot-electron signal is well described by a single exponential decay with a time constant of 120 ± 5 fs. The dynamics of hot electrons with high excess energies in GaAs has been studied extensively [29,46]. The hot-electron packets photoinjected into the Γ valley are transformed into hot-electron ensembles quasiequilibrated only in momentum space at ultrafast rates of the order of 10 fs, and the energy relaxation of the ensembles takes place as a whole on a longer time scale with rates dependent only on the excess energy [29,46]. The rate given by the inverse of time constant of 120 fs for hot electrons with $E_{cb} = 0.88$ eV in the inset agrees very well with that extrapolated from an extensive data set obtained for hot electrons with $E_{cb} < 0.80$ eV at 90 K [46].

Interestingly, the decay of slow component of EX photoemission is governed by the time constant which is almost the same as that of hot electrons. As to the decay characteristics of the fast component of the EX photoemission, it is not possible to determine the decay time without quantitative analysis, which takes into account a finite width of cross correlation between pump- and probe pulses of 75 fs. We analyze the decay dynamics of the EX photoemission later in Sec. IV C.

We carried out excitation spectroscopy for the EX photoemission by tuning $h\upsilon_{pump}$ from 2.80 to 3.06 eV. Similar to the result in Fig. 2(c), photoemission from hot electrons in the Γ valley are weak, but the intense EX photoemission peak is commonly detected under excitation with these photon energies at the time frame of $\Delta t > 0$. Figure 5(a) shows the maximum intensity of EX photoemission as a function of $h\upsilon_{pump}$. The yield of the EX photoemission depends on $h\upsilon_{pump}$, and the largest enhancement occurs at $h\upsilon_{pump} = 2.95 \pm 0.05$ eV. Figure 5(b) shows the magnitude of $k_{||}$ that gives the EX-

photoemission peak. The $k_{||}$ is 0.183 ± 0.007 Å^{-1}, and it does not depend on $h\upsilon_{\text{pump}}$.

In the excitation spectroscopy, the 3ω pulses of the fundamental beams of photon energy $h\upsilon_0$ were used as the probe-light pulses, while the 2ω pulses were used as pump-light pulses. For $h\upsilon_{\text{pump}}$ ranging from 2.80 to 3.06 eV, the intense EX photoemissions were detected at the time frame of $\Delta t > 0$, with showing decay profiles similar to that shown in Fig. 4. Therefore, the EX state is generated by 2ω pulses and the state is probed by 3ω pulses. The magnitude of $E_K(\vec{k})$ of photoelectrons ionized from a given initial state is dependent on $h\upsilon_{\text{probe}}(= 3h\upsilon_0)$, as seen in Eq. (1). In order to exclude this $h\upsilon_{\text{probe}}$-dependent effect, the initial-state energy $E_I(\vec{k})$ for photoemission was evaluated using Eq. (1), and is plotted as a function of $h\upsilon_{\text{pump}}(= 2h\upsilon_0)$ in Fig. 5(c), together with the photoemission peak from the CBM measured at $\Delta t = 10$ ps. It is clear that the photoemission from the CBM gives $E_I(\vec{k}) = 1.50$ eV referenced to the VBM irrespective of $h\upsilon_{\text{pump}}$. It gives the magnitude of the band-gap energy at 90 K, being consistent with the results reported previously [47].

For the EX photoemission, the magnitude of $E_I(\vec{k})$ determined using Eq. (1) is also constant, which is 0.88 eV above the CBM (2.38 eV above the VBM). However, the initial-state energy determined using Eq. (1) gives correct meaning only when the state is defined by the IQP picture, just like the CBM peak. When the photoemission originates from exciton photoionization, the magnitude of the initial-state energy shown in Fig. 5(c) is not appropriate to specify the state responsible for the photoemission, as the $E_K(\vec{k})$ in this case is given by Eq. (3). The identification of the initial state of the EX photoemission is the main issue in this study, and we discuss it extensively in the next section. Here we emphasize only that the EX state is a well-defined electronic state in GaAs, specified by the characteristic energy and momentum.

IV. DISCUSSION

As described in Sec. III, the EX photoemission is the most striking feature in the photoemission from GaAs excited at ~3 eV. The EX state is highly localized in the momentum space around $k_{||} = 0.183$ Å^{-1} in the two-dimensional plane of the BBZ defined by axes of [110] and [001] and shows ultrafast temporal evolution. The relaxation processes are unique, which are largely different from those of hot electrons in the CB generated by excitation with $h\upsilon_{\text{pump}} < 2.5$ eV. The formation of the EX state is excitation-wavelength dependent, and the resonant enhancement occurs at $h\upsilon_{\text{pump}} = 2.95 \pm 0.05$ eV. Below we discuss the origin of the EX photoemission based on extensive quantitative analysis of the present results and results available in literature.

A. EX photoemission and photoemission from hot electrons in the bulk- and surface-electronic states

1. Conduction-band states along the Γ-L line in the BBZ and the EX state

In order to differentiate the EX photoemission and photoemission from hot electrons in the bulk CB, we first identify experimentally the relaxation pathways of hot electrons in-

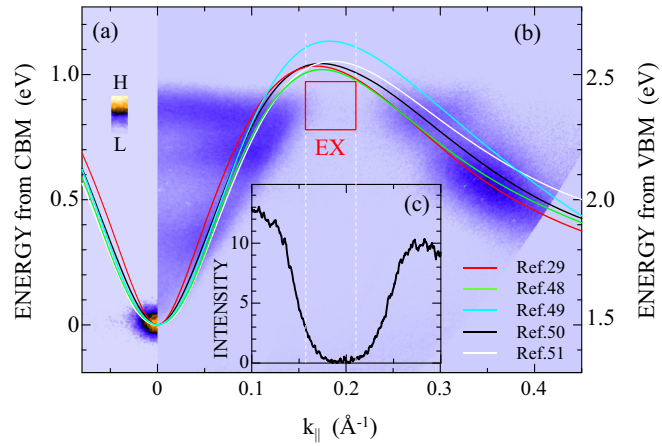

FIG. 6. (a) Photoemission image of CBM photoemission measured at $\Delta t = 10$ ps. (b) The map of transient hot-electron distribution during relaxation at Δt ranging from 10 to 267 fs under 2.48-eV excitation. In (a) and (b), the square root of photoemission intensities specified by a color scale are plotted as a function of $k_{||}$ and E_{cb}. The solid curves with different colors show the theoretical results of conduction-band dispersion along the Γ-L line obtained by different theoretical methods in Refs. [29,48–51]. The red rectangle labeled EX shows the energy and momentum region where the EX photoemission is excited intensely under excitation with photon energies from 2.8 to 3.1 eV. (c) The photoemission intensity under 2.48-eV excitation integrated in the energy range from 0.85 to 0.91 eV as a function of $k_{||}$. The intensity is plotted in a linear scale for $k_{||}$ ranging from 0.1 to 0.3 Å^{-1}.

jected into the CB within the detection plane defined by the [110] and [001] axes of GaAs. Figures 3(a)–3(f) have given snap shots of transient hot-electron populations during the relaxation toward the L_1 and the CBM under 2.48-eV excitation. In the measurements, hot electrons populated at 0.95 eV above the CBM have been captured. We sum up all of these snapshots to obtain the map showing possible routes along which hot electrons are relaxing below $E_{\text{cb}} = 0.95$ eV. The result is shown in Fig. 6(b); Fig. 6(a) shows a photoemission image measured at $\Delta t = 10$ ps in order to indicate the energy position of the CBM in the map. In the figures, the square root of the photoemission intensity is plotted as a function of $k_{||}$ and E_{cb} in order to show clearly the regions with weak intensities.

As is well known, the determination of $k_{||}$ fixes a point on the two-dimensional SBZ; the momentum $k_{\perp}$ normal to the surface can have a value anywhere along the rod extending into the three-dimensional BBZ [44]. Despite the composite features in off-normal emission, it is instructive to compare the result with the CB dispersion along the Γ-L line to which extensive theoretical studies have given the quantitative dispersion characteristics. Under the experimental geometry given in Fig. 2(d), the states along the Γ-L line contribute to off-normal emissions from typical high-symmetry points.

In Figs. 6(a) and 6(b), the solid curves with different colors show theoretical results of CB dispersion calculated using different methods [29,48–51]. Although all results give qualitatively similar dispersions, they are different quantitatively in several points. The $k_{||}$ that gives the saddle point along the

Γ-L line is ranging from 0.169 to 0.186 Å^{-1}, and the energy at the saddle point changes from 1.02 to 1.13 eV above the CBM. Nevertheless, all band-structure calculations have given smooth changes in energy around the saddle point without any singular points. In Fig. 6(b), the region (EX region) of energy and momentum for the EX photoemission have been marked by the red rectangle. It is clear that the EX region deviates significantly from the CB dispersions predicted from the IQP band structures. In particular, at $k_{||} = 0.183$ Å^{-1} the energy is lower than the result of the band-structure calculation in Ref. [48] that gives the lowest energy around the saddle point.

In Fig. 6(c), the k-resolved photoemission intensity at $E_{cb} = 0.88 \pm 0.03$ eV is plotted as a function of $k_{||}$ ranging from 0.1 to 0.3 Å^{-1} in a linear scale. It is clear that the intensity, or the amount of transient hot-electron population, is practically zero at the EX region; the intensity is less than those at L and Γ valleys by a factor of 10^{-2}. Therefore, hot electrons with $E_{cb} = 0.95$ eV generated by 2.48-eV excitation cannot be relaxed into the EX region during the relaxation toward the CBM. As studied in in Refs. [29] and [46], photoinjected hot electrons with high excess energies are quasiequilibrated in the momentum space of a whole BBZ at ultrafast rates of the order of 10 fs. Therefore, a transient hot-electron population in the short time frame is determined mainly by the density of state of the CB at a given region specified by both energy and momentum. The result in Fig. 6(c) shows that there are no density of states of the CB at the EX region. In view of the specific feature of hot-electron relaxation with high excess energy in GaAs, the result in Fig. 6 shows clearly that the EX photoemission cannot be ascribed to the photoemission from any states of the bulk CB transiently populated during hot-electron relaxation.

Furthermore, as shown in Figs. 3 and 4, the unique characteristics of relaxation of EX photoemission are qualitatively different from those of hot electrons populated in the CB at similar energy range and momentum space. Therefore, we can conclude that the initial state of the EX photoemission is nothing to do with photoemissions from hot electrons transiently populated in the bulk CB states; it has a different origin.

2. Surface-specific electronic states and the EX state

On cleaved (110) surfaces of GaAs, only a small amount of surface relaxations of cations and anions are observed, with keeping the dimension of the unit cell, which contains a pair of one cation and one anion in the topmost surface layers, thus being nonpolar and with an atomic structure close to the bulk [41]. The surface atoms are relaxed normal to the surface from their positions in a bulklike layer; anions move inward by ≈0.2 Å, while cations move outward by ≈0.7 Å. These structural relaxations are confined mostly within the first two layers of the surface with a typical depth of ≈1 Å. However, the surface relaxation leads to the well-defined surface-specific electronic states including the As-derived occupied surface band (A_5) and the Ga-derived unoccupied band (C_3) [41]. Here we discuss possible correlations between the EX state and the surface-specific electronic states. As the EX state is resonantly excited at $h\upsilon_{pump} = 2.95$ eV, and is specified by the initial-state energy of 0.88 eV above the CBM, surface

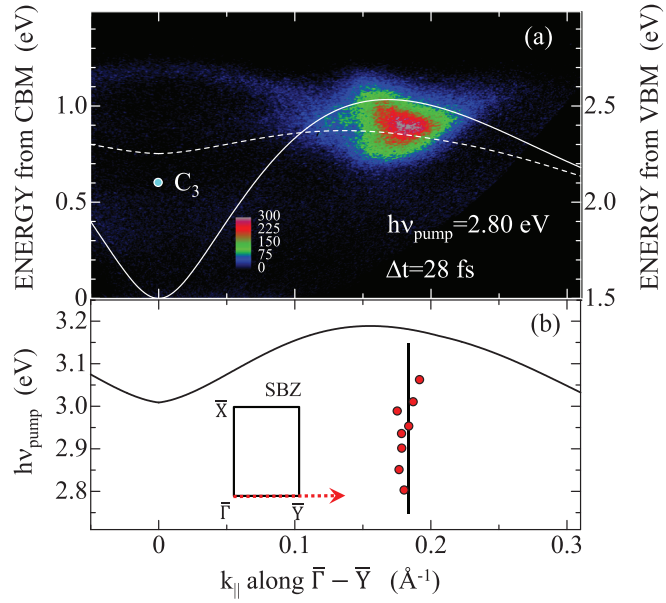

FIG. 7. (a) Two-dimensional map of photoemission from GaAs excited by 2.80-eV photons as a function of $k_{||}$ and E_{cb}. The solid curve is the bulk CB dispersion along the Γ-L line, and the broken curve displays the theoretical dispersion of the C_3 unoccupied surface state in Ref. [58]. The solid point labeled C_3 at the $\bar{\Gamma}$ ($k_{||} = 0$) shows the result of inverse photoemission spectroscopy for the C_3 unoccupied surface state (after Ref. [54]). (b) The relation between the excitation-photon energy and $k_{||}$ for the surface optical transitions evaluated using theoretical results in Ref. [58]. Red circles are replots of data shown in Fig. 5(b). The inset shows the surface Brillouin zone of the GaAs(110)−(1 × 1), with the red arrow showing the direction in the experimental measurement.

states with energetics similar to those of the EX state are examined extensively.

The surface states have been studied extensively by optical spectroscopy and inverse photoemission spectroscopy. It has been reported that the surface-specific optical transition occurs at 2.8–2.9 eV over a substantial part of the SBZ [52,53]. The photon-energy range is close to that of the bulk E_1 transitions where the EX photoemission is excited efficiently as shown in Fig. 5(a). Also, inverse photoemission spectroscopy studies reported the energy of unoccupied C_3 surface band to be 2.1 eV above the VBM at the $\bar{\Gamma}$ [54–56]. The energy of the C_3 band at the $\bar{\Gamma}$ is also close to the initial-state energy (2.38 eV above the VBM) of the EX photoemission determined in Fig. 5(c). Despite these similarities in the energetics between the EX photoemission and photoemission from the C_3 surface band, one cannot ascribe the EX photoemission to the photoemission from hot electrons transiently populated at the normally unoccupied C_3 surface state, since qualitatively different features are obvious in the momentum-resolved characteristics of the two photoemission processes as discussed below.

In Fig. 7(a), the two-dimensional photoemission map excited by 2.80-eV photons is shown as a function of $k_{||}$ along the $\bar{\Gamma}$-$\bar{Y}$ direction and the E_{cb} (the initial-state energy referenced to the VBM is also shown in the right axis). The solid curve is the bulk CB dispersion along the Γ-L line. The photon

energy of 2.80 eV was particularly chosen to differentiate the EX photoemission and surface-state photoemissions. The onset of the surface-optical transitions energy is 2.8 eV, which occurs at the $\bar{X}$ of the SBZ as identified before [56–58]. Under the present experimental geometry used to measure the result shown in Fig. 7(a), no photoemissions at $\bar{X}$ can be detected [see Fig. 2(d) and the inset of Fig. 7(b)]. However, the intense EX photoemission is detected at $E_{cb} = 0.89$ eV and $k_{||} = 0.181$ Å^{-1} along the $\bar{\Gamma}$-$\bar{Y}$ under 2.80-eV excitation, being qualitatively contradictory to the consequences of surface-state transitions.

As evidenced experimentally and theoretically, the A_5 and C_3 surface states on the GaAs(110)$-(1 \times 1)$ surface show prominent dispersive features along the $\bar{\Gamma}$-$\bar{Y}$ as well as the $\bar{\Gamma}$-$\bar{X}$ directions [41,57,58]. The broken curve in Fig. 7(a) is the theoretical dispersion of the C_3 unoccupied surface state along $\bar{\Gamma}$-$\bar{Y}$ [58], which serves as the initial state of surface-state photoemission when the C_3 band is transiently occupied. The solid point labeled C_3 at the $\bar{\Gamma}$ ($k_{||} = 0$ Å^{-1}) represents the result of inverse photoemission spectroscopy for the C_3 band [54]. A reasonable agreement can be seen between the experimental and theoretical results at the $\bar{\Gamma}$ within the combined experimental and theoretical error [58]. Because of the dispersive features of A_5 and C_3 states, optical transitions in the surface electronic states take place at different $k_{||}$'s, depending on $h\upsilon_{pump}$'s. Using the theoretical results of Ref. [58], we can evaluate the relation between $h\upsilon_{pump}$ and $k_{||}$ for the surface optical transitions. The estimated relation is plotted by the solid black curve in Fig. 7(b). It is clear that the magnitude of $k_{||}$ along $\bar{\Gamma}$-$\bar{Y}$, at which a transition takes place to a final state on the surface C_3 band, changes continuously from 0 to 0.31 Å^{-1} depending on $h\upsilon_{pump}$.

The red circles in Fig. 7(b) replot the experimental results of $k_{||}$ for the EX photoemission excited by $h\upsilon_{pump}$ shown in Fig. 5(b). In strong contrast to the consequence of dispersive characteristics of surface transitions, the EX photoemission shows a constant $k_{||}$ (0.183 ± 0.007 Å^{-1}), irrespective of $h\upsilon_{pump}$ ranging from 2.8 to 3.1 eV. The essentially different characteristics in the momentum space between the EX photoemission and photoemission from the C_3 surface state excludes definitively the possibility that the EX photoemission might be the surface-state photoemission on GaAs(110)$-(1 \times 1)$.

As seen in Fig. 7(a), as well as Fig. 2(c), several weak photoemission peaks can be detected in the Γ-valley region, together with the intense EX photoemission. The intensities are typically weaker than the EX photoemission by a factor of 10^{-3}. As described in the Appendix, most of the weak photoemission peaks are due to hot-electron states in the bulk CB; no surface-specific photoemission peaks could be resolved and detected. As described in Sec. II, energy of final states generated by pump and probe pulses has been restricted to be lower than 8 eV from the Fermi level. At the energy range, the length of inelastic mean free path is larger than 30 Å, much longer than the depth of the (1×1) surface layer of ~ 1 Å. This volume effect may be the main reason why the surface-specific photoemission peaks, including one from the C_3 surface band, could not be detected in the present photoemission study.

B. EX photoemission and exciton photoionization

As discussed above, the EX state is neither hot electrons formed in the bulk CB nor those in the surface-specific electronic states. The EX state is highly localized in the momentum space including BBZ along the Γ-L line, and has a well-defined energy above the VBM. The formation efficiency is sensitively dependent on excitation photon energy; the largest enhancement occurs at the photon energy of 2.95 eV. Previous studies have suggested strong excitonic effects at the excitation-photon energy [12,17,18]. Therefore, the saddle-point excitons formed at the E_1-critical point is a promising candidate of EX photoemission. When the sample is excited by laser pulses at the exciton resonance, the light field induces an excitonic polarization coherently. The probe pulse with sufficiently large photon energy then generates photoemission characteristic of the coherent excitonic polarization. Recent theoretical studies on exciton photoionization have revealed several important aspects which differ significantly from those for one-electron photoemission scheme [24–28], as described in the Introduction. Here we examine critically the relation between the present results and the theoretical consequences of exciton photoionization.

1. Energy-resolved characteristics of EX photoemission

As seen in images of Figs. 2(c) and 3(g)–3(l), the EX photoemission and hot-electron photoemissions coexist around the saddle point of the CB dispersion curve. The overlap of the two types of photoemission makes the spectroscopic analysis less transparent, although the intensities of hot-electron photoemissions are weak. In Fig. 8(a), we show the photoemission map at $\Delta t = -5$ fs under 2.98-eV excitation on expanded scales of E_K and $k_{||}$. The energy scale is given by the kinetic energy of photoelectrons, as the initial-state energy given by the IQP picture has no physical meaning in exciton photoionization processes [see Eq. (3)]. Although the photoemissions from hot electrons (marked HE) are present [59], together with the EX photoemission, the hot-electron signals are well separated from the EX photoemission. Therefore, it is possible to analyze quantitatively the spectral shape of the fast component of the EX photoemission with the least ambiguity.

Figure 8(b) shows the angle-integrated photoemission spectrum; it shows the peak kinetic energy at 1.38 eV [60]. As will be described in Sec. IV C, the decay time of the fast component of EX photoemission is 11 ± 0.5 fs, which corresponds to energy broadening of 60 meV. Therefore, we calculated the Lorentzian line shape with this width and convolved it with respect to a finite experimental energy resolution of 60 meV. The thin solid curve in Fig. 8(b) is the result of this convolution, showing reasonable agreement with the experimental spectrum. Careful inspection of the experimental spectrum, however, reveals an asymmetry with respect to energy; the low-energy part is suppressed, while the high-energy part is enhanced. Although the asymmetry may reflect some interactions involved in the initial and/or final states of photoemission, we leave this problem open until more precise determination of the asymmetry is made.

The exciton-photoionization theory predicts the photoelectron-kinetic energy given by Eq. (3). When we

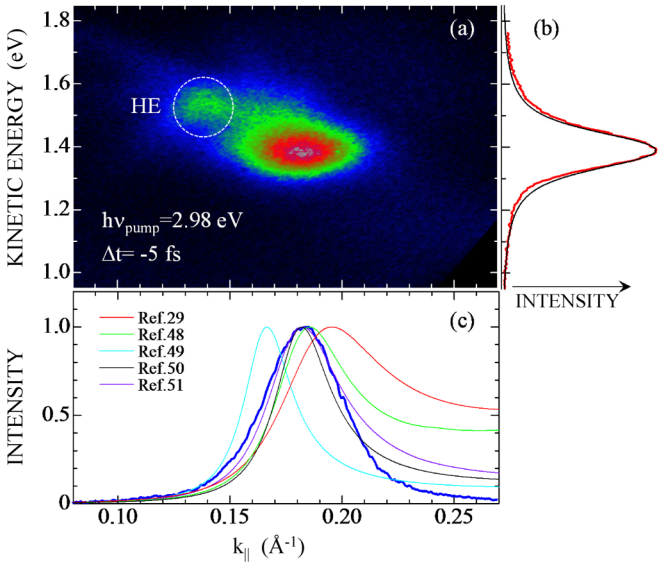

FIG. 8. (a) Part of photoemission image measured at $\Delta t = -5$ fs under excitation at 2.98 eV in expanded scales of $k_{||}$ and the kinetic energy of photoelectrons. Photoemissions highlighted by a circle labeled HE are due to hot electrons in the conduction band, and are excluded in the spectral-shape analysis of the EX photoemission. (b) The angle-integrated spectrum of EX photoemission, red curve, and a theoretical Lorentzian spectrum with a lifetime broadening of 60 meV, black curve (see the text). (c) The momentum-resolved intensity of energy-integrated EX photoemission (solid blue curve). Thin solid curves with different colors show theoretical wave functions given by Eq. (4) calculated using the results of band structure calculations in Refs. [29,48–51].

identify the $E_{EX} = 2.95$ eV, which is the peak photon energy for EX-photoemission excitation shown in Fig. 5(a), the recoil energy $E_R(-\vec{k})$ by the hole restoration is estimated to be 0.57 eV using $E_K = 1.38$ eV determined above. In the sudden approximation of photoemission [61], $E_R(-\vec{k})$ is determined by the dispersion relation of the valence band [25,26]. A previous photoemission spectroscopy study on the valence-band dispersion in GaAs has shown that valence-band state at $k_L = 0.32$ Å^{-1} ($k_{||} = 0.183$ Å^{-1}) along the Γ-L line is -0.60 eV with respect to the VBM [62]. The magnitude of 0.57 eV for $E_R(-\vec{k})$ obtained by Eq. (3) is in a reasonable range of the valence-band dispersion, being consistent with the exciton photoionization model [63].

2. Momentum-resolved characteristics of EX photoemission

The spectrum in Fig. 8(c) shows the energy-integrated and momentum-resolved photoemission intensity as a function of $k_{||}$. In the photoionization of excitons, the photoemission intensity specified by $\hbar\vec{k}$ and E_K is proportional to $|f(\vec{k}, -\vec{k})|^2$ [24–28]. Therefore, the peak of k-resolved photoemission intensity indicates the wave vector of the IQB Bloch state that contributes most strongly to the exciton wave function. The EX photoemission shows the maximum intensity at $k_{||} = 0.183$ Å^{-1}, which corresponds to $k_L = 0.32$ Å^{-1}. As stated above, the off-normal photoemission detected experimentally at a given $k_{||}$ is a superposition of many contributions from such states that are projected on the one-dimensional cut along the $\bar{\Gamma}$-$\bar{Y}$ direction of the SBZ. The spectrum in Fig. 8(c) possibly includes this effect of superposition. Despite the composite features in the off-normal emission, it is instructive to analyze the $k_{||}$-resolved intensity of EX photoemission in terms of IQP electronic structures along the Γ-L direction to which valence- and conduction-band dispersions have been calculated.

Although the exact form of wave function of SPEs is not easily formulated theoretically, mainly because of a finite (short) lifetime of the state, an approximate wave function has been obtained by an extrapolation method under contact-potential approximation in Ref. [25]:

$$f(\vec{k}, -\vec{k}) = A/\{E_C(\vec{k}) - E_V(-\vec{k}) - E_{EX} + i\Gamma_{EX}\}, \quad (4)$$

where A is a constant, $E_C(\vec{k}) - E_V(-\vec{k})$ gives the energy difference between the CB and VB at an electron (hole) wave number $\tilde{k}$ ($-\vec{k}$), and Γ_{EX} is the lifetime broadening of the excitonic state. Using the results of the band-structure calculations, the one-dimensional cut along the Γ-L line of exciton wave function can be calculated. For this purpose, we use the "scissor shift approximation" [64,65] to set the $E_G = 1.50$ eV for all band-structure calculations used here. The solid curves in Fig. 8(c) show the results of $|f(\vec{k}, -\vec{k})|^2$ with $E_{EX} = 2.95$ eV and $\Gamma_{EX} = 60$ meV for theoretical band structures given in Refs. [29,48–51]. It is clear that the calculated spectral shape depends sensitively on the details of band-structure calculations. However, it is also clear that a sharp peak feature is predicted around the saddle point of the first CB for all theoretical results. Therefore, we can conclude that the experimentally determined energy- and momentum-resolved features of EX photoemission are well described in terms of exciton photoionization model.

Based on the results and analysis described in this section, we conclude that the initial state of EX photoemission is the saddle-point exciton formed along the Γ-L line. This conclusion is certainly consistent with the results of previous study on spectral line-shape analysis on the E_1 transition in GaAs at low temperatures [12]. The electron-hole pair states around $k_L = 0.32$ Å^{-1}contribute most effectively to the exciton wave function. Although we cannot determine the binding energy of the SPE, it has been suggested theoretically that it is larger than that of the Γ-point exciton in GaAs [25].

C. Dynamical properties of the saddle-point exciton

As shown in Fig. 4, the decay of EX photoemission is bimodal; the fast decay follows the slow-decay component which shows spectroscopic properties similar to those of the fast one. Based on the conclusion we have reached in Sec. VI B that the EX photoemission is due to the photoionization of SPEs, we discuss the dynamical properties of the SPE, an excitonic state formed at energy higher than the E_G. In order to gain more quantitative information on the dynamics of the SPEs, we first analyze the decay characteristics using a simple method described below.

The semiconductor Bloch equations certainly provide a suitable theoretical framework for analyzing optical properties of semiconductors [5,66]. However, the equations have to

be supplemented with an appropriate treatment of the complicated scattering terms involved in pulse excited semiconductors. Unfortunately, we were unable to obtain the details of the scattering processes under the present temporal and energy resolutions of the measurements. Also, the dephasing process of coherent excitonic polarization formed above the E_G is influenced by a strong interaction with a continuum of unbound electron-hole pair states, resulting in completely different mechanisms of dephasing from those of the Γ excitons formed at energies below E_G. How to describe the dephasing process of high-energy excitonic polarization is not trivial. Here we use a simple optical Bloch equation with neglecting all Coulomb interaction terms in the semiconductor Bloch equations; we obtain only phenomenological quantities of population decay time T_1 and polarization dephasing time T_2. The failure of a simple rate equation model to describe the time response for coherent excitation has been discussed extensively in Ref. [67].

Following the method in Refs. [39,67], we model the time-resolved photoemission process by two sequential excitation steps. The first step corresponds to the resonance excitation from the ground state $|1\rangle$ to the excitonic state $|2\rangle$. Under coherent resonance conditions, $T_2 = 2T_1$. The second step corresponds to the exciton photoionization leading to the final state $|3\rangle$ at which the electron is photoemitted. As the temporal response of the final-state population is not of relevance, we restrict the analysis to a simple two-level system consisting of $|1\rangle$ and $|2\rangle$. The second photoionization step is evaluated by simply convoluting the calculated population of the state $|2\rangle$ with probe pulses.

As seen in Fig. 4, the EX photoemission shows a bimodal decay including the fast and slow components. We assume that the rise of slow component is governed by the decay of fast component. So, we analyze the fast component by the optical Bloch equation, and describe the slow component by a rate equation with the population-rise time being the same as the population decay time T_1 for the fast component [39]. We discuss the assumption later.

Typical results of the analysis are displayed and compared with experimental results in Fig. 9(a). The solid blue curve shows the fast component for $T_1 = 11$ fs, while the broken curve shows the slow component of the EX photoemission with a decay time constant τ of 120 fs. The sum of two components shown by the thin solid-black curve describes well the experimental results. We have found that experimental decay of the EX photoemission is best described by $T_1 = 11 \pm 0.5$ fs and $\tau = 120 \pm 10$ fs. As well known in previous time-resolved spectroscopy, the dephasing processes in semiconductors are carrier-density dependent [6,7,68]. In order to examine the effects of excitation density on the population decay time determined above, we analyzed the results of EX photoemission obtained for the ρ_0 ranging from 0.73×10^{16} to 5.5×10^{17} cm^{-3}. In this excitation-density range, the intensity of the EX photoemission increased in proportion to ρ_0, while the decay times of both fast and slow components did not show any density-dependent changes; they showed the same magnitudes within the error range given above. The results reveal that the dephasing process of coherent excitonic polarization is not affected strongly by the carrier-density dependent scattering and screening processes

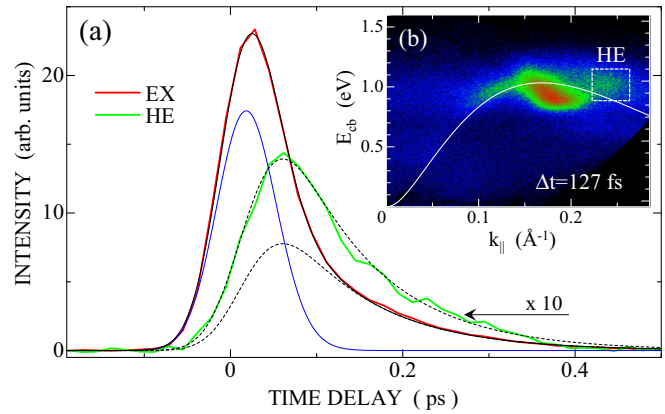

FIG. 9. (a) Analysis of temporal evolution of total intensity of EX photoemission. The solid red curve is the experimental total EX-photoemission intensity, and the solid blue and broken black curves show the best-fitted fast and slow components of EX photoemission. The sum of fast- and slow-component intensities shown by the thin black curve is compared with the experimental result. The solid green curve shows temporal evolution of photoemission intensity integrated in the rectangle region labeled HE in (b). (b) Part of photoemission image at $\Delta t = 127$ fs under 2.98-eV excitation; the square root of photoemission intensity is mapped as a function of $k_{||}$ and E_{cb} to enhance weak-intensity features. In order to specify hot electrons relaxing along the CB dispersion curve clearer, the energy is scaled in terms of E_{cb}. The solid curve is the conduction-band dispersion along the Γ-L line.

in the excitation range studied, and suggest that the dephasing is governed by other interactions of SPEs.

As seen in Fig. 4, it is clear that the peak kinetic energy of slow component of EX photoemission shifts upward by 0.05 eV than the fast component. It is also clear that the dispersive features of fast and slow components show some differences as seen in Figs. 3(g)–3(l). Therefore, two different states of saddle-point excitons are formed depending on the time after short-pulse excitation.

As supplemental information to understand the difference of the two EX states, we study the temporal correlation between the EX photoemission and hot-electron photoemission generated by 2.98-eV excitation. Figure 9(b) shows the photoemission image at $\Delta t = 127$ fs at a more expanded scale than Fig. 3(k). In the image, the square root of the intensity is plotted to enhance the features of weak-intensity peaks due to hot electrons in the CB. Hot electrons relaxing along the dispersion curve of CB are clearly visible together with the EX photoemission that is well-localized in the momentum space. This result reconfirms experimentally that the slow component of EX photoemission is not due to photoionization of hot electrons in the CB, although the decay time constants are quite similar as seen in Fig. 4. We pay our attention to the hot-electron signals specified with a rectangle labeled HE in Fig. 9(b), as they are well separated from the EX photoemission in the momentum space; no overlap with the EX peak is expected. The intensity integrated within the rectangle is plotted by the solid green curve as a function of Δt in Fig. 9(a). Importantly, the temporal change of hot-electron photoemission intensity shows the same dynamics

(shown by the broken curve) as that of the slow component of the EX photoemission, revealing that the formation time of hot electrons is identical to the population decay time of the fast component of the EX photoemission. The result can be regarded as a direct piece of evidence indicating that the decay of the fast component of the EX state leads to the generation of hot electrons in the CB.

The exciton states formed far above the E_G are degenerate with a continuum of unbound electron-hole pair states, resulting in the strong interaction between the discrete and continuum states. Such an interaction has been studied theoretically by Fano [15,69]. The coherent excitonic polarization resonantly excited by laser pulses may then be transferred into unbound pair states with a rate dependent on the strength of the interaction. As shown in Fig. 9, the decay of the fast component of EX photoemission leads to the generation of hot electrons along the CB dispersion curve. Therefore, we can conclude that the fast decay of the EX photoemission corresponds to the process of "autoionization" [15], or the transfer from the coherently formed excitonic state to unbound electron-hole pair states. The analysis in Fig. 9 has shown that the time constant is 11 ± 0.5 fs. For the Γ excitons formed below the E_G in semiconductors, the decay of macroscopic polarization resonantly excited is governed by the dephasing time typically in picosecond range [5–8]. The much shorter decay time of SPEs can be ascribed to the strong electronic interaction between SPEs and unbound electron-hole pair states.

On the other hand, the similar excitonic state survives up to 500 fs. We propose that the long-lived excitonic states are formed by incoherent processes via back reactions from unbound pair states to the excitonic state; excitonic and free-carrier states reach quasiequilibrium rapidly. The long-lived EX peak is characterized by a higher kinetic energy, with substantial changes in the dispersive feature in the k space as seen in Figs. 3(g)–3(l). This suggests that the wave functions of excitons formed in the incoherent process is not the same as that formed resonantly. The ultrafast changes in distributions of free-carrier states in energy and momentum spaces may cause incoherent formation of excitonic states with time-dependent wave functions. Time-dependent plasma screening [70] may also contribute to the difference in the wave functions of SPEs formed in the incoherent process. Although elucidation of the incoherent process of exciton formation is an important issue to understand dynamical interaction between excitons and free-carrier states, exact analysis of spectral line shape of the slow EX photoemission was not possible, because of significant overlap of photoemission with hot-electron photoemission.

V. SUMMARY

We have studied the electronic structure and dynamical properties of saddle-point excitons in GaAs formed under E_1-resonance excitation around 3.0 eV, using time- and angle-resolved photoemission spectroscopy. The unique photoemission peak, which is resonantly enhanced under excitation at 2.95 eV, shows significant deviation from the conduction-band states, and exhibits a unique relaxation dynamics. The EX photoemission has been identified to the photoemission from the saddle-point excitons in GaAs, based on the analysis of energy- and momentum-resolved spectroscopic features. It has been shown that the photoemission from the saddle-point exciton is governed by recoil effects of the conjugated hole that restores the valence-band states, as proposed by the theory of exciton photoionization. Using momentum-resolved capability of photoemission spectroscopy, the amplitudes of IQP Bloch states of which the exciton is composed have been determined. Also, using ultrafast time-resolved capability, we have revealed that coherently generated SPEs decay with a time constant of 11 fs, which corresponds to the rate of autoionization processes from the excitons to unbound electron-hole pair states in GaAs. This work has demonstrated that the time- and angle-resolved photoemission spectroscopy provides far deeper insight into the nature of the excitonic states formed at high-energy region above the E_G in semiconductors.

ACKNOWLEDGMENTS

We thank K. Nasu, J. Kanasaki, and J. Güdde for valuable discussions. This work was supported by the Japan Society for the Promotion of Science (JSPS) KAKENHI Grant No. 24000006.

APPENDIX: PHOTOEMISSION PEAKS IN THE Γ VALLEY UNDER 3.0-eV EXCITATION

Together with the unique EX photoemission, some photoemission peaks with weak intensities are detected in the Γ valley under excitation around 3 eV, as seen in Figs. 2(c) and 3(g)–3(l). Here we discuss the photoemission processes of these peaks (Γ-valley peaks hereafter) to clarify the whole process in GaAs under photoexcitation with photon energies around 3.0 eV.

In order to show clearly the features of Γ-valley photoemissions, a photoemission image, measured at $\Delta t = 33$ fs under 3.06-eV excitation, is displayed in Fig. 10(a); the square root of the intensity is plotted as a function of $k_{||}$ and E_K. The normal emission spectrum ($k_{||} = 0 \pm 0.01$ Å^{-1}) of the image is shown in Fig. 10(b), where three peaks, denoted A, B, and C, are resolved. In the figures, the kinetic energy is used to specify the photoelectrons, as the photoemission processes responsible for the peaks are different. In our time-resolved photoemission measurements using two laser pulses with different frequencies $\omega_1 (= 2\omega)$ and $\omega_2 (= 3\omega)$, photoemission processes change, depending on the time delays of ω_2 pulses with respect to ω_1 pulses. For $\Delta t < 0$, the intermediate states (or the initial states of photoemission) are formed by ω_2 pulses and photoemissions are probed by ω_1 pulses, while for $\Delta t > 0$ the intermediate states are formed by ω_1 pulses and photoemissions are probed by ω_2 pulses. In the time frame near $\Delta t = 0$, both processes coexist, together with possible coherent processes by ω_1 and ω_2 pulses because of finite temporal widths of two light pulses.

In Fig. 11, temporal changes of the photoemission intensities of peaks A, B, and C are displayed. It is clear that the peak B shows the maximum at $\Delta t = 15$ fs following a rapid decay within 100 fs of excitation. Therefore, the intermediate state is generated by 2ω-light pulses, and photoionization is induced by 3ω-light pulses. On the other hand, peak A

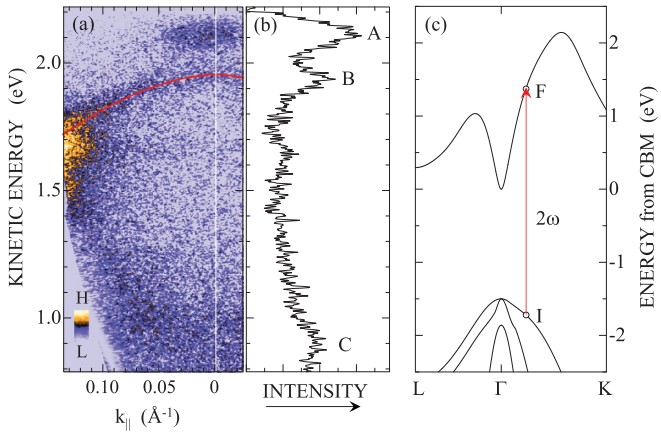

FIG. 10. (a) Part of photoemission image measured at $\Delta t =$ 33 fs under 3.06-eV excitation; the square root of the intensity is mapped as a function of $k_{||}$ and E_K. The red curve is a result of analysis of the dispersion of peak B defined in (b) (see the text). (b) The spectrum of surface-normal photoemission ($k_{||} = 0 \pm 0.01$ Å^{-1}) in the image in (a). Three peaks, denoted A, B, and C, are resolved. (c) The electronic band structure of GaAs along the L-Γ-K lines in Ref. [29]. The scissor shift approximation was applied to set the $E_G = 1.50$ eV. The red arrow shows an optical transition from point I on the heavy-hole valence band to point F on the first CB along the Γ-K line by 3.06-eV light pulses.

precedes peak B, showing the maximum at $\Delta t = -10$ fs with a tail extending to the negative Δt region. The result shows that peak A is due to the photoemission process, in which the intermediate states are generated by 3ω-light pulses following photoionization by 2ω-light pulses. The temporal change of peak C shows a complicated dynamics; it increases at longer positive Δt, together with the rise extending in the negative Δt region. The enhancement at the positive Δt region reflects the dynamics of hot electrons generated by 2ω-light pulses and probed by 3ω-light pulses. The energy relaxation of hot electrons with high excess energies toward the CBM is presumed to be the main cause of the intensity enhancement.

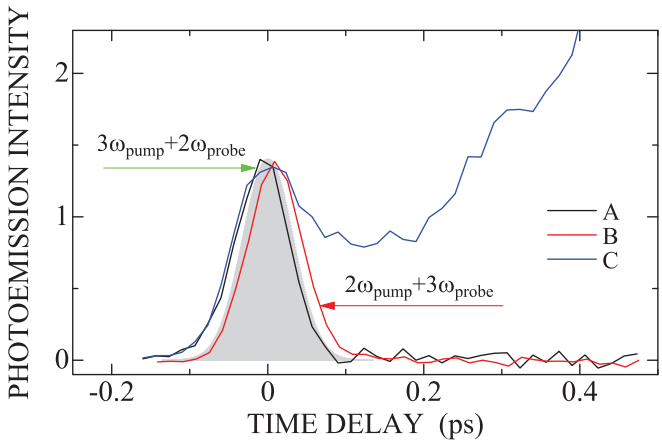

FIG. 11. Temporal evolution of photoemission intensities of peaks A, B, and C defined in the surface-normal photoemission in Fig. 10(b). The grey peak shows the cross-correlation trace between pump-and probe pulses.

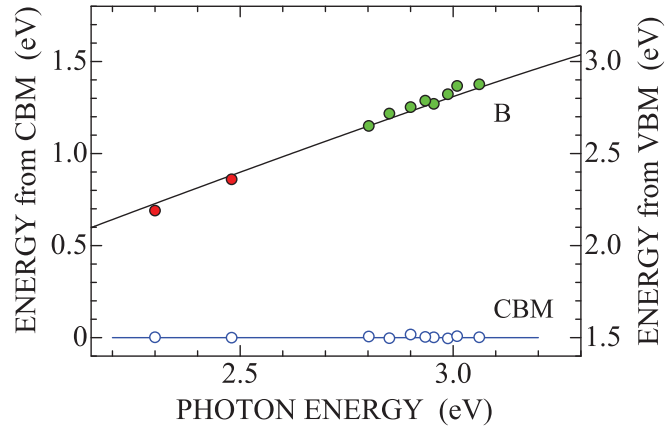

FIG. 12. The initial-state energy of photoemission peak B, green circles, as a function of pump-photon energy. The energies of the highest-energy peaks in the Γ valley under 2.30- and 2.48-eV excitation are shown by red circles. The solid curve shows the evaluated energy of the final state of optical transitions from heavy-hole valence band to the conduction band as a function of $h\upsilon_{\text{pump}}$. The blue circles show the initial-state energy of CBM photoemission.

On the other hand, the initial rise of peak C at $\Delta t < 0$ shows essentially the same temporal evolution as peak A. Therefore, it is most likely that peak C near $\Delta t = 0$ is due to hot electrons injected by 3ω pulses following photoionization by 2ω pulses.

With leaving the assignment of peaks A and C as later topics, we describe first the characteristics of peak B, which shows a highly dispersive feature. The initial state of photoemission for peak B is generated by 2ω-light pulses following photoionization by 3ω-light pulses, as shown in Fig. 11. Therefore, the kinetic energy of photoelectrons of peak B can be correlated with the $E_{\text{I}}(\vec{k})$ using Eq. (1) with $h\upsilon_{\text{probe}} = 3h\upsilon_0$. In Fig. 12, the energy of the initial state of photoemission (the final state of optical transition) of peak B at the $\bar{\Gamma}$ is plotted as a function of $h\upsilon_{\text{pump}}$ by green circles. It increases with increasing $h\upsilon_{\text{pump}}$, ranging from 1.1 to 1.4 eV above the CBM. We identify the initial state of the photoemission of peak B to be the hot electrons excited from the heavy-hole valence band to the first CB along the Γ-K line in BBZ by 2ω pulses, based on the following results.

The band structure of GaAs calculated in Ref. [29] is shown in Fig. 10(c), which displays the dispersions of the first CB and three valence bands along the L-Γ-K line. Under the present experimental geometry, the normal emission comes from the CB states along the Γ-K line. The band structure in Fig. 10(c) predicts that for $h\upsilon_{\text{pump}} = 3.06$ eV the optical transitions from the heavy-hole band can generate hot electrons along the Γ-K line at the same energy region as the initial state of photoemission of peak B ($E_{\text{cb}} = 1.38$ eV). The initial (point I) and final (point F) states of the optical transition by 3.06-eV excitation is indicated by red arrow in Fig. 10(c). Because of the energy and momentum conservations in the transition processes, the initial states of optical transitions at the VB along Γ-K are lowered in energy typically about 0.2 eV from the VBM. Using the band structure, we estimated the energy of the final state of optical transitions as a function of $h\upsilon_{\text{pump}}$, and plotted the results by solid black curve in Fig. 12.

The predicted values agree well to the observed energy of the peak B. In Fig. 12, the initial state energies of the highest photoemission peaks at the $\bar{\Gamma}$ under 2.30 and 2.48 eV [see Figs. 2(a) and 2(b)] are also plotted by red circles. The peaks are due to photoionization of the hot electrons generated by optical transitions from the heavy-hole valence band to the first CB as identified previously [29,39]. These points are well registered on the theoretical values of the initial states of photoemission evaluated above, substantiating our assignment of the origin of peak B. Furthermore, the polarization selection rule tells that the transition from the heavy-hole band to the first CB at the Σ point is allowed for the *s*-polarized light, but is prohibited for the *p*-polarized light [45]. In fact, when the same sample is excited by *p*-polarized light, peak B is completely missing, being consistent with our identification.

Under the present experimental geometry, the off-normal emission includes significant contributions from states along the Γ-L direction. The optical transitions from initial VB states, specified by the wave vector k_K and k_L generate hot electrons at the CB states specified by the same set of k_K and k_L. For the states with finite k_L, the energies of the final states of optical transitions are lower than the states at Σ ($k_L = 0$) by amounts determined by the heavy-hole dispersion along the Γ-L line. The hot-electron populations thus formed are photoemitted at a finite $k_{||}$ determined by the amount of k_L. In order to estimate this effect, we simply added the heavy-hole dispersion along the Γ-L direction to the energy in the normal photoemission spectrum. The estimated dispersion is plotted by the solid red curve as a function of $k_{||}$ in Fig. 10(a), which describes well the detected dispersion of peak B.

As identified above, peaks A and C are due to initial states generated by 3ω-light pulses following the photoionization by 2ω-light pulses. By using Eq. (1) with $h\nu_\mathrm{probe} = 2h\nu_0$, we estimate the initial state energies to be 3.05 (4.55) eV for peak A and 1.83 (3.38) eV for peak C above the CBM (VBM) for the spectrum in Fig. 10(b). Peak A shows a narrow momentum distribution centered at the $\bar{\Gamma}$. Therefore, the states along the Γ-K line are mainly responsible for the peak. Interestingly, the excitation of peak A has a threshold energy; it is excited only for $h\nu_\mathrm{pump}(= 3h\nu_0)$ larger than 4.48 eV. In the band structure of GaAs, the energy of $E_0{}'$ is 4.50 eV [12], which may coincide with the threshold energy of peak A. Therefore, it is most likely that the initial state responsible for peak A is the second CB state around the Γ populated by optical transitions by 3ω pulses from the VB states near the VBM. The peak C is characterized by weak intensity and by widely spread distributions in energy and momentum spaces. At $h\nu_\mathrm{pump} > 4$ eV , many transitions at different points in BBZ are possible. Because of these complexities, we could not identify the initial states of peak C, unfortunately.

As described above, most of the photoemission peaks in the Γ valley can be ascribed successfully to the hot-electron states in the bulk CB; no surface-specific photoemission peaks could be resolved and detected. We presume that this is due to the enhanced bulk sensitivity in the photoemission measurements under the present experimental conditions where final-state energies generated by pump and probe pulses have been restricted to be lower than 8 eV from the Fermi level; the length of inelastic mean free path of electrons is much longer than the depth of the (1×1) surface layer.

[1] P. Y. Yu and M. Cardona, *Fundamentals of Semiconductors: Physics and Materials Properties* (Springer, Berlin, 1996).

[2] Y. Toyozawa, *Optical Processes in Solids* (Cambridge University Press, New York, 2003).

[3] J. C. Phillips, Phys. Rev. **136**, A1705 (1964).

[4] J. C. Phillips and B. O. Seraphin, Phys. Rev. Lett. **15**, 107 (1965).

[5] S. W. Koch, M. Kira, G. Khitrova, and H. M. Gibbs, Nat. Mater. **5**, 523 (2006).

[6] J. Shah, *Ultrafast Spectroscopy of semiconductors and Semiconductor Nanostructures*, 2nd ed. (Springer, Berlin, 1999).

[7] V. M. Axt and T. Kuhn, Rep. Prog. Phys. **67**, 433 (2004), and references therein.

[8] F. Rossi and T. Kuhn, Rev. Mod. Phys. **74**, 895 (2002).

[9] E. O. Kane, Phys. Rev. **180**, 852 (1969), and references cited therein.

[10] D. E. Aspnes and A. A. Studna, Phys. Rev. B **7**, 4605 (1973).

[11] S. F. Pond and P. Handler, Phys. Rev. B **8**, 2869 (1973).

[12] P. Lautenschlager, M. Garriga, S. Logothetidis, and M. Cardona, Phys. Rev. B **35**, 9174 (1987).

[13] P. Lautenschlager, M. Garriga, L. Vina, and M. Cardona, Phys. Rev. B **36**, 4821 (1987).

[14] J. C. Phillips, in *The Optical Properties of Solids*, edited by J. Tauc (Academic, New York,1966), pp.155–184.

[15] U. Fano, Phys. Rev. **124**, 1866 (1961).

[16] W. Hanke and L. J. Sham, Phys. Rev. Lett. **43**, 387 (1979).

[17] L. X. Benedict, E. L. Shirley, and R. B. Bohn, Phys. Rev. B **57**, R9385 (1998).

[18] M. Rohlfing and S. G. Louie, Phys. Rev. B **62**, 4927 (2000), and references therein.

[19] L. Chiodo, J. M. García-Lastra, A. Iacomino, S. Ossicini, J. Zhao, H. Petek, and A. Rubio, Phys. Rev. B **82**, 045207 (2010).

[20] A. Riefer, F. Fuchs, C. Rödl, A. Schleife, F. Bechstedt, and R. Goldhahn, Phys. Rev. B **84**, 075218 (2011).

[21] K. F. Mak, J. Shan, and T. F. Heinz, Phys. Rev. Lett. **106**, 046401 (2011).

[22] K. F. Mak, F. H. da Jornada, K. He, J. Deslippe, N. Petrone, J. Hone, J. Shan, S. G. Louie, and T. F. Heinz, Phys. Rev. Lett. **112**, 207401 (2014).

[23] C. Poellmann, P. Steinleitner, U. Leierseder, P. Nagler, G. Plechinger, M. Porer, R. Bratschitsch, C. Schüller, T. Korn, and R. Huber, Nat. Mater. **14**, 889 (2015).

[24] E. Perfetto, D. Sangalli, A. Marini, and G. Stefanucci, Phys. Rev. B **94**, 245303 (2016).

[25] H. Ohnishi, N. Tomita, and K. Nasu, Int. J. Mod. Phys. B **32**, 1850094 (2018).

[26] A. Rustagi and A. F. Kemper, Phys. Rev. B **97**, 235310 (2018).

[27] D. Sangalli, E. Perfetto, G. Stefanucci, and A. Marini, Eur. Phys. J. B **91**, 171 (2018).

[28] A. Rustagi and A. F. Kemper, Phys. Rev. B **99**, 125303 (2019).

[29] H. Tanimura, J. Kanasaki, K. Tanimura, J. Sjakste, N. Vast, M. Calandra, and F. Mauri, Phys. Rev. B **93**, 161203(R) (2016).

[30] R. J. Elliott, Phys. Rev. **108**, 1384 (1957).

[31] J. J. Hopfield, Phys. Rev. **112**, 1555 (1958).

[32] H. Tanimura, K. Tanimura, and P. H. M. van Loosdrecht, Phys. Rev. B **100**, 115204 (2019).

[33] M. Weinelt, M. Kutschera, T. Fauster, and M. Rohlfing, Phys. Rev. Lett. **92**, 126801 (2004).

[34] E. Varene, L. Bogner, C. Bronner, and P. Tegeder, Phys. Rev. Lett. **109**, 207601 (2012).

[35] J.-C. Deinert, D. Wegkamp, M. Meyer, C. Richter, M. Wolf, and J. Stähler, Phys. Rev. Lett. **113**, 057602 (2014).

[36] X. Cui, C. Wang, A. Argondizzo, S. Garrett-Roe, B. Gumhalter, and H. Petek, Nat. Phys. **10**, 505 (2014).

[37] X.-Y. Zhu, J. Electron Spectrosc. Relat. Phenom. **204**, 75 (2015).

[38] A. Amo, M. D. Martín, and L. Viña, A. I. Toropov, and K. S. Zhuravlev, Phys. Rev. B **73**, 035205 (2006).

[39] J. Kanasaki, H. Tanimura, and K. Tanimura, Phys. Rev. Lett. **113**, 237401 (2014).

[40] K. Oura, V. G. Lifshits, A. A. Saranin, A. V. Zotov, and M. Katayama, *Surface Science: An Introduction* (Springer, Berlin, 2003).

[41] W. Mönch, *Semiconductor Surfaces and Interfaces* (Springer, Berlin, 1995).

[42] M. Weinelt, M. Kutschera, R. Schmidt, C. Orth, T. Fauster, and M. Rohlfing, Appl. Phys. A **80**, 995 (2005).

[43] G. W. Gobeli and F. G. Allen, Phys. Rev. **137**, A245 (1965).

[44] E.W. Plummet and W. Eberhardt, *Advances in Chemical Physics* (Wiley, New York, 1982).

[45] D.W. Niles, D. Rioux, and H. Höchst, Phys. Rev. B **46**, 12547 (1992).

[46] J. Sjakste, N. Vast, G. Barbarino, M. Calandra, F. Mauri, J. Kanasaki, H. Tanimura, and K. Tanimura, Phys. Rev. B **97**, 064302 (2018).

[47] I. Vurgaftman, J. R. Meyer, and L. R. Ram-Mohan, J. Appl. Phys. **89**, 5815 (2001).

[48] J. R. Chelikowsky and M. L. Cohen, Phys. Rev. B **14**, 556 (1976).

[49] S. Richard, F. Aniel, and G. Fishman, Phys. Rev. B **70**, 235204 (2004).

[50] Y-S. Kim, M. Marsman, G. Kresse, F. Tran, and P. Blaha, Phys. Rev. B **82**, 205212 (2010).

[51] B. D. Malone and M. L. Cohen, J. Phys.: Condens. Matter **25**, 105503 (2013).

[52] V. L. Berkovits, I. V. Makarenko, T. A. Minashvili, and V. I. Safarov, Solid State Commun. **56**, 449 (1985).

[53] S. Selci, A. Cricenti, F. Ciccacci, A. C. Felici, C. Goletti, Z. Yong, and G. Chiarotti, Surf. Sci. **189/190**, 1023 (1987).

[54] D. Straub, M. Skibowski, and F. J. Himpsel, Phys. Rev. B **32**, 5237 (1985).

[55] H. Carstensen, R. Claessen, R. Manzke, and M. Skibowski, Phys. Rev. B **41**, 9880 (1990).

[56] F. J. Himpsel, Surf. Sci. Rep. **12**, 3 (1990).

[57] B. Reihl, T. Riesterer, M. Tschudy, and P. Perfetti, Phys. Rev. B **38**, 13456 (1988).

[58] X. Zhu, S. B. Zhang, S. G. Louie, and M. L. Cohen, Phys. Rev. Lett. **63**, 2112 (1989).

[59] We searched the optical transitions that can induce the well-isolate hot-electron population indicated by the dotted circle in Fig. 8(a), using the band structure calculated in Ref. [29]. The transition from the light-hole valence band to the conduction band at $k_{\mathrm{L}} = 0.238$ Å^{-1} can be such a transition that generates hot electrons with $E_K = 1.53$ eV and $k_{||} = 0.138$ Å^{-1}.

[60] For determining the angle-integrated spectral functions of EX peak, we analyzed photoemission spectra resolved with respect to $k_{||}$ obtained at different Δt's in order to exclude contributions from coexisting hot-electron components along the CB dispersion line. However, the intensities at $E_K > 1.5$ eV may include a possible error of $\pm 10\%$.

[61] A. Damascelli, Z. Hussain, and Z.-X. Shen, Rev. Mod. Phys. **75**, 473 (2003).

[62] T.-C. Chiang, J. A. Knapp, M. Aono, and D. E. Eastman, Phys. Rev. B **21**, 3513 (1980).

[63] Band-structure calculations in Refs. [29,48–51] have shown that the energy of the heavy-hole band at $k_L = 0.32$ Å^{-1} ($k_{||} = 0.18$ Å^{-1}) is -0.41 ± 0.03 eV with respect to the VBM, which predicts $E_R(-\vec{k})$ smaller than the experimental value of 0.57 eV by 0.15 eV. The difference may be related to several issues at different levels to be clarified further. First, the state-resolved valence-band dispersions have not yet been established along the Γ-L line in GaAs; the dispersions of heavy-hole and light-hole bands could not be resolved in the experimental results in Ref. [62]. The accurate determination of the dispersions with energy resolution better than 100 meV gives crucial information on the difference between experimental and theoretical $E_R(-\vec{k})$. Second, the valence-band dispersion only along the Γ-L direction may underestimate the amount of recoil energy upon hole restoration in the photoionization of SPEs, as the SPE has a three-dimensional nature; electron-hole pair states along the two transverse directions perpendicular to the Γ-L direction contribute to the wave function significantly as shown theoretically in Ref. [9]. In the present study, the measurement of k-resolved photoemission intensity is restricted only along the $\bar{\Gamma}$-$\bar{Y}$ direction of the SBZ. Simultaneous measurements both along $\bar{\Gamma}$-$\bar{Y}$ and $\bar{\Gamma}$-$\bar{X}$ directions may give important knowledge about the three-dimensional nature of SPEs and hence the contributions of the electron-hole pair states along the transverse directions to the exciton wave function. Third, we have followed theoretical results of exciton photoionization in Refs. [25,26], in which the photoemission process has been treated in terms of the one-electron picture under the sudden approximation. The sudden approximation is in principle applicable only to electrons with high kinetic energy (more than 100 eV) as discussed in Ref. [61]. On the other hand, it is only $\sim$1 eV in the present case. Also, the temporal width of probe-light pulse is 50 fs, which probes the electronic processes in the photoemission only in a short time frame. Therefore, it is far from trivial how to describe the photoionization process of excitons under the present experimental conditions. Although the issues described above include important fundamental problems in photoemission processes probed by low-energy probe light with a short temporal width, they are beyond the scope of the present study; we leave them as important open questions in future studies.

[64] K. A. Johnson and N. W. Ashcroft, Phys. Rev. B **58**, 15548 (1998).

[65] M. Schlüter and L. J. Sham, Adv. Quantum Chem. **21**, 97 (1990).

[66] H. Haug and S. W. Koch, *Quantum Theory of the Optical and Electronic Properties of Semiconductors* (World Scientific, Singapore, 1990).

[67] T. Hertel, E. Knoesel, M. Wolf, and G. Ertl, Phys. Rev. Lett. **76**, 535 (1996).

[68] P. C. Becker, H. L. Fragnito, C. H. Brito Cruz, R. L. Fork, J. E. Cunningham, J. E. Henry, and C. V. Shank, Phys. Rev. Lett. **61**, 1647 (1988).

[69] Optical excitation in a system where a discrete resonance couples with transitions into a continuum displays an asymmetric spectrum caused by constructive and destructive interferences of excitation paths, as formulated in Ref. [15]. The excitation spectrum of EX photoemission shown in Fig. 5(a) may include such an effect. However, a limited spectrum range and rather large errors of data points do not allow us to carry out any meaningful analysis of the spectral line shape.

[70] R. Huber, F. Tauser, A. Brodschelm, M. Bichler, G. Abstreiter, and A. Leitenstorfer, Nature (London) **414**, 286 (2001).